Tomographic volumetric bioprinting of 3D pancreatic cancer models

Viola Sgarminato[1, 2, *], Jorge Madrid-Wolff[2, *], Antoine Boniface[2, *], Gianluca Ciardelli[1], Chiara Tonda-Turo[1], Christophe Moser[2]

1. Department of Mechanical and Aerospace Engineering, Politecnico di Torino, Italy
2. Laboratory of Applied Photonics Devices, Ecole Polytechnique Fédérale de Lausanne, Switzerland

*. These authors contributed equally to this work

1. Abstract

Pancreatic ductal adenocarcinoma (PDAC) is the most frequent type of pancreatic cancer, one of the leading causes of cancer-related deaths worldwide. PDAC is marked by a dense, fibrous tumor microenvironment, in which stromal fibroblasts surround the cancerous ductal epithelial cells. The crosstalk between pancreatic cells and the surrounding fibroblasts leads to inflammation and stiffening of the surrounding tissue, which is believed to hinder anti-cancer drugs' uptake and effectiveness. *In vitro*, fully human models of the pancreatic cancer microenvironment are needed to foster the development of new, more effective therapies; but it is still challenging to make these models anatomically and functionally relevant. Here, we use tomographic volumetric bioprinting, a novel method to fabricate cell-laden viable constructs within less than a minute, to produce anatomically relevant fibroblast-laden gelatine methacrylate-based pancreatic models, including a duct and an acinus. We then seeded human pancreatic ductal epithelial (HPDE) cells, wild type or cancerous, into these models and evaluated the progression of the constructs for several days after printing. We show that the 3D pancreatic duct models remain viable for up to 14 days after bioprinting. We used immunofluorescence to evaluate the surrounding fibroblasts' activation by quantifying the relative expressions of alpha smooth muscle actin (αSMA) vs. actin in the fibroblasts. αSMA is known to be overexpressed in inflamed tumor-associated fibroblasts. We show that αSMA expression is significantly higher in fibroblasts co-cultured with cancerous than with wild-type HPDE cells, that this expression increases with time, and that it is higher in fibroblasts that lay closer to HPDE cells than in those deeper into the model. These models could potentially be used in drug development or to shed light on the early progression of the disease.

2. Introduction

Pancreatic cancer represents one of the leading causes of cancer-related death worldwide, with a five-year survival rate below 9%[1,2]. Among all types of known pancreatic cancer subtypes, pancreatic ductal adenocarcinoma (PDAC) is the most frequent, accounting for 93% of cancers arising from the pancreas[3]. The absence of clear symptoms in the first stages of PDAC evolution reduces the chances to make an early diagnosis, resulting in a poor clinical prognosis. Indeed, only approximately 10% of the patients are eligible for surgical resection in combination with adjuvant and/or pre-operative therapy, since the majority of cases present spread metastases and extended lesions at diagnosis[4,5].

Moreover, the unique bioarchitecture of the pancreatic tumor microenvironment (TME) weakens the effectiveness of the current treatments that, despite the advances in the discovery of new therapeutic strategies, result insufficient to treat this particularly aggressive pathology[4,6,7].

In detail, the PDAC microenvironment is composed of approximately 90% desmoplastic stroma consisting of collagen, fibronectin, fibrillar collagen and hyaluronic acid (HA)[8]. This dense stromal tissue creates a hypoxic environment and plays a key role in disease progression and drug resistance, constituting a barrier which impedes therapeutics access. The stroma arises from the excessive extracellular matrix (ECM) deposition by pancreatic stellate cells (PSCs) that are responsible for the intense desmoplastic reaction occurring within the tissue surrounding the cancer cells[9,10]. More precisely, in healthy tissue PSCs are located in the periacinar space around the acinar and ductal epithelial cells that constitute the pancreatic functional unit (Fig. 1a), responsible for the secretion of the digestive enzymes and the region where the pancreatic intraepithelial neoplasia (PanIN) develops[4,11,12]. PanIN is the early precursor lesion which progresses to the development of PDAC through mutation of specific genes in epithelial cells (Fig. 1b).

Although the alterations that give rise to PanIN precursor lesions are still to be clarified, hallmarks associated to pathology onset have been identified. Indeed, the oncogene KRAS in the epithelial cells have been reported as the more frequent mutation leading to the progression of PanIN[13]. Besides mutation in epithelial tissue genome, PDAC formation is also characterized by the desmoplastic reaction induced by cancer cells. Therefore, during the pancreatic carcinogenesis, the PSCs, that are in a quiescent state and exhibit a star-shaped morphology, activate in response to inflammatory cues and cancer cells-derived factors, acquiring a myofibroblasts-like phenotype which is characterized by spindle-shaped morphology[14] (Fig.1b). Typically, activated PSCs assemble in a core-shell like structure surrounding the cancer cells and start to interact with them by generating a complex autocrine and paracrine signaling interplay[15,16]. In this intricate framework, the stromal components actively interact with pancreatic cancer cells through different ways that significantly affect gene expression patterns, metabolic activities, invasion/metastasis phenomena and resistance mechanisms[17]. In particular, the activated PSCs released cytokines such as the Interleukin 6 (IL-6) and growth factors (e.g., TGF-β), leading to an increase in inflammatory cues fostering the mutation of the oncogene KRAS in the epithelial cells and the progression from PanIN to PDAC[15,18] (Fig. 1b).

The understanding of such dynamic phenomena involved in PDAC-stroma crosstalk might expand the knowledge of the pathology and consequently discover innovative biological targets. Indeed, even though important risk factors can contribute to the development of the pancreatic cancer (like smoking, obesity, type 2 diabetes, chronic pancreatitis, and alcoholism[19]) and although the mechanisms of evolution from the neoplasia are well documented[20,21], the alterations causing the early lesions still remain unclear[22]. Therefore, the understanding of pancreatic cancer raises interests among the scientific community, currently developing efficient PDAC *in vitro* models in order to detect the disease earlier and design effective therapies thus improving patients' prognosis[23–28]. Although recent works have shown the possibility of modeling the PDAC microenvironment *in vitro*[23,24,26,29–34], the tumor-stroma interplay remains arduous to be replicate and monitor in functionally effective models[35–38]. Heterotypic 3D spheroids, patient-derived organoids, cancer-on-a-chip platforms, and 3D biofabricated constructs are the currently available bioengineered 3D models mimicking the pancreatic tumor-stroma interplay[16]. However, only a few novel studies

in literature focus on the development of biomimetic platforms reproducing the microanatomy (in terms of 3D architecture and cellular composition) of the exocrine pancreas and lack to resemble the native compartmentalized architecture of tumor microenvironment that is widely recognized to affect cell functionality and cancer-cell response to therapeutics[39–41]. In particular, the gland complex geometry has been reproduced in simplified ways by employing different techniques like viscous fingering and extrusion-based methods[42–45], that have disadvantages such as the low reproducibility, throughput and shape fidelity. These limitations can be overcome by the use of volumetric bioprinting (VBP) which represents an emerging light-based technology capable of fabricating 3D constructs with high-resolution and complex geometries rapidly[46–49]. Indeed, this technique permits to print hollow structures without the need for support and in a very short building time (down to a few tens of seconds compared to tens of minutes for layer-by-layer approaches) [47]. Furthermore, one of the main advantages of VBP is the cell-friendly procedure lying in the one-step manufacturing process which reduces the stress experienced by cells as compared to other multistep techniques such as the common solvent-casting method[50]. More specifically, VBP consists of illuminating a photosensitive cell-laden hydrogel with visible light from multiple angles, using a sequence of tomographic back projections of the desired object[51–53], leading to the photopolymerization of the material. We adopt VBP to develop a fully human 3D *in vitro* model resembling the physiological acinar- and ductal-like structure of the pancreatic gland (Fig. 1c). In particular, a gelatin methacrylate hydrogel (GelMA) has been *ad hoc* prepared, tailoring the polymer and the photoinitiator concentrations, and loaded with human fibroblasts (stromal cells) to mimic the stromal compartment. We fabricated numerous fibroblast-laden structures by VBP (Fig. 1c,d). Then, we introduced healthy human pancreatic ductal epithelial cells (HPDE-WT) or stably expressing the KRAS oncogene (HPDE-KRAS) inside the construct's cavity and monitored the co-culture overtime (Fig. 1e). We analyzed the tumor-stroma crosstalk effect measuring the appearance of a myo-fibroblast phenotype by quantifying expression of alpha smooth muscle actin (αSMA) proteins in fibroblasts (Fig. 1f).

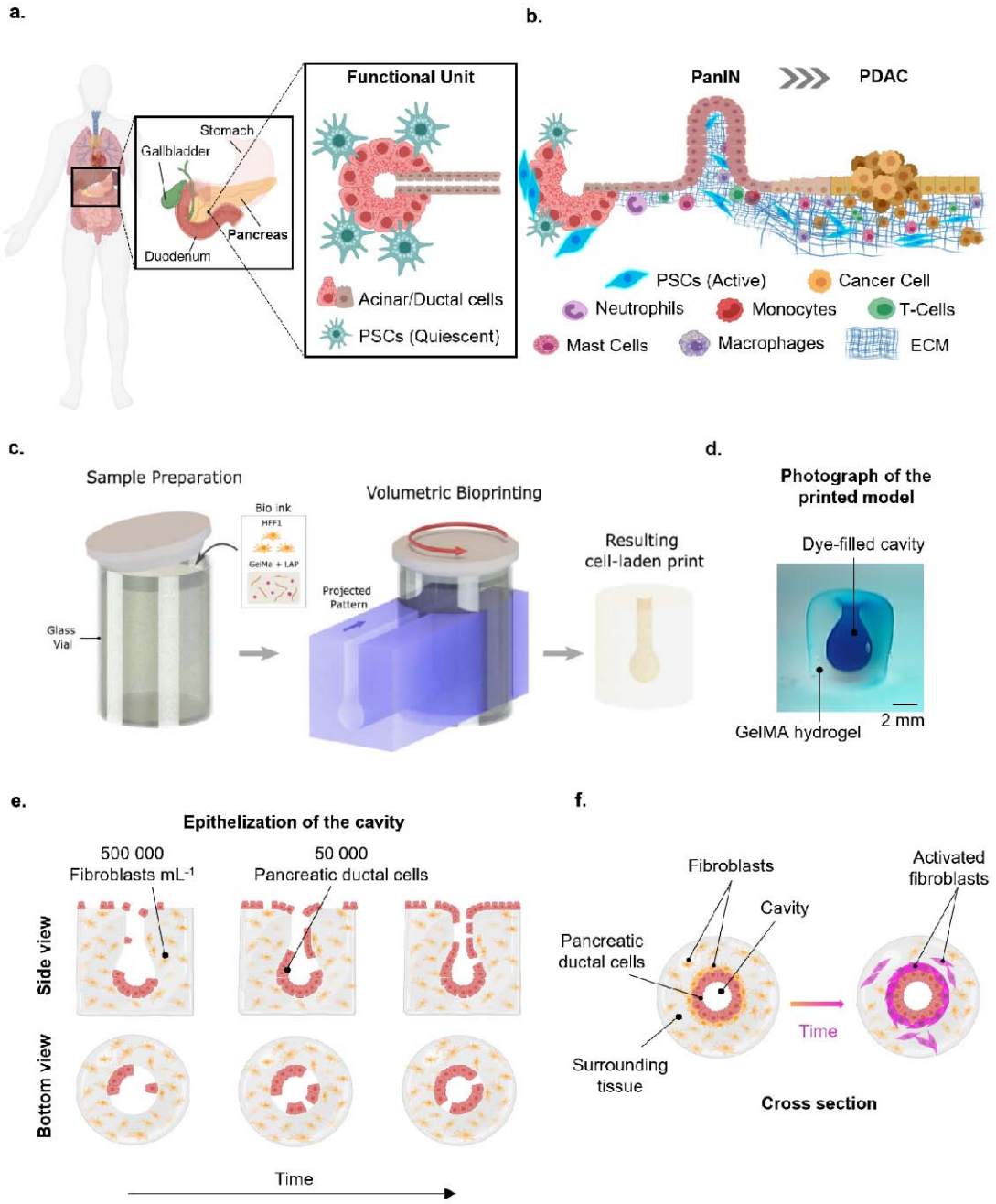

Fig. 1. Experimental pipeline for tomographic volumetric bioprinting of pancreatic cancer models. **a**. Pancreatic cancer typically occurs within the functional unit of exocrine pancreas, composed by epithelial cells (acinar and ductal cells) surrounded by pancreatic stellate cells (PSCs). **b.** Schematic representation of pancreatic intraepithelial neoplasia (PanIN) progression inspired from Liot et al.[13]. Particular focus is made on PSCs activation which triggers the desmoplastic response. **c.** In tomographic volumetric bioprinting, a gelatin metacryloyl (GelMA) 5% solution in cell medium containing the photoinitiator lithium phenyl-2,4,6-trimethylbenzoylphosphinate (LAP) 0.16 mg mL^{-1} and 0.5 million fibroblasts (HFF1) mL^{-1} is poured into glass vials and printed. A cell-laden construct

that mimics the functional unit of exocrine pancreas is obtained. **d**. Photograph of a bioprinted construct (immersed in water) with the cavity filled with a glycerol-based blue dye (for visualization purpose only). **e**. Human Pancreatic Ductal Epithelial (HPDE) cells, healthy or cancerous, can be injected into fibroblast-laden bioprinted constructs, where they will attach and coat the inner surface of the duct with time. **f.** To recapitulate fibroblast-associated inflammation or activation, the interaction between HPDE cells stably expressing the KRAS oncogene (HPDE-KRAS) and the surrounding fibroblasts is monitored by measuring the expression of **α**SMA versus actin in the cytoskeletons of the latter. (Figure drawn using Biorender.com).

3. Results

3.1 Fabrication of exocrine pancreatic units through VBP

The fabricated constructs followed a ductal geometry, with an acinus of larger diameter at the end (sup. video 1). This geometry is challenging to fabricate without employing support structures or without joining two compartments. In VBP, we projected a set of tomographic light patterns into cell-laden GelMA (5% w/v in DMEM w/o phenol red + 0.5 million fibroblasts mL^{-1}) in which we added the photoinitiator at a low concentration (0.16 mg mL^{-1}) (Fig.2). The selected concentration of the photoinitiator allows the crosslinking of GelMA upon visible light irradiation at 405 nm wavelength (Fig. 2a,b) and it is low enough to reduce cytotoxicity and light absorption. The photorheological test proved the sol-gel transition of GelMA as a result of light irradiation (Fig. 2b). The increment of storage modulus (G') until reaching a stable plateau at 0.4 KPa indicates the elastic response of the material, whose viscoelastic properties are comparable to that of pancreatic tissue[54] (sup. fig. 1). The light-scattering effect caused by the presence of cells within the gel causes a loss of resolution in the constructed object, such as a resulting obstructed duct or an incomplete acinus. However, by performing a numerical correction of the light dose that uses quantitative information on the light scattering[47], we obtained an improvement in shape fidelity and resolution of the printed structures (Fig. 2c,d). Features of the final geometry, such as the wall thickness and the duct diameter, were optimized to guarantee printability and maximize anatomical relevance. This is because there is a trade-off between structural integrity and cell viability, as metabolic activity in cells within hydrogels is known to decrease with distance from the outer borders of the hydrogel[55].

3.2 Viability of exocrine pancreatic units

We assessed the viability of cells within the bioprinted pancreatic ductal models first by monitoring the state of the fibroblasts. Fig. 3a shows fluorescence microscopy images of constructs 24 hours, 72 hours, 7 days, and 14 days after printing. Live cells, shown in blue, had been stained with calcein-AM, a membrane-permeant dye that is converted into a fluorescent calcein by intracellular esterases. Dead cells, shown in orange, had been stained with ethidium homodimer-1, which is a membrane-impermeant high-affinity nucleic acid stain that is weakly fluorescent until bound to DNA. The micrographs show the region around the duct, 300 μm deep inside the constructs, with fibroblasts assuming an elongated shape and fully colonizing the inner walls of the duct over time. Micrographs also demonstrate that most cells survived after the printing process and that they were homogenously distributed within the hydrogels at 24h. Then, cell proliferation and maturation occurred over two weeks as

confirmed by the metabolic activity of fibroblasts which increased with time. Indeed, Fig. 3b shows fluorometric measurements of the CellTiter-Blue cell-viability assay ($n_{GelMA\ +\ cells}$ = 7, n_{GelMa} = 7), in which resazurin is reduced by metabolic reactions in the cells to resorufin, a fluorescent molecule. Higher fluorescence intensity indicates higher cell viability. We see a significant ($p < 0.0001$), marked increase in metabolic activity 72 to 96 hours after printing, which is sustained at least until 9 days after printing. This significant increment in cell viability at 96h is probably associated to the cell recovery from stress that the biofabrication process may cause. GelMA hydrogels have residual free radicals left after gelation, which can themselves account for the reduction of rezasurin[56]. We control for this effect by measuring the fluorescence intensity also in bioprinted GelMA hydrogels without cells, and observe they have a reduction 2 orders of magnitude lower than the one in cell-laden hydrogels (Fig. 3b).

In the meantime, we also evaluated the capacity of HPDE cells to epithelize the walls of the cavity (duct and acinus) of the bioprinted constructs. For this, we injected HPDE cells into the GelMA bioprinted structures without fibroblasts. Fig. 3c shows microscopy images from a Live/Dead assay (calcein-AM and ethidium homodimer-1) of HPDE cells 24, 48, and 72 hours after seeding into the cavity of the constructs (sup. video 2). Dashed lines indicate the contour of the cavity. The images, which correspond to the intensity sum over planes along 500 µm of the microscope's optical axis, show that HPDE cells cover larger extents of the duct walls with time and produce a lining of > 1 mm^2 72 hours after seeding. When co-cultured with fibroblasts, HPDE cells may progress more slowly, probably due to the competition for resources in cell medium, but still form large linings and invade the bulk, as shown with arrows in Fig. 3d, 3f and sup. fig. 2. In Fig. 3e multi-channel fluorescence microscopy images of the duct wall of a fibroblast-laden construct co-cultured with HPDE-KRAS cells are reported.

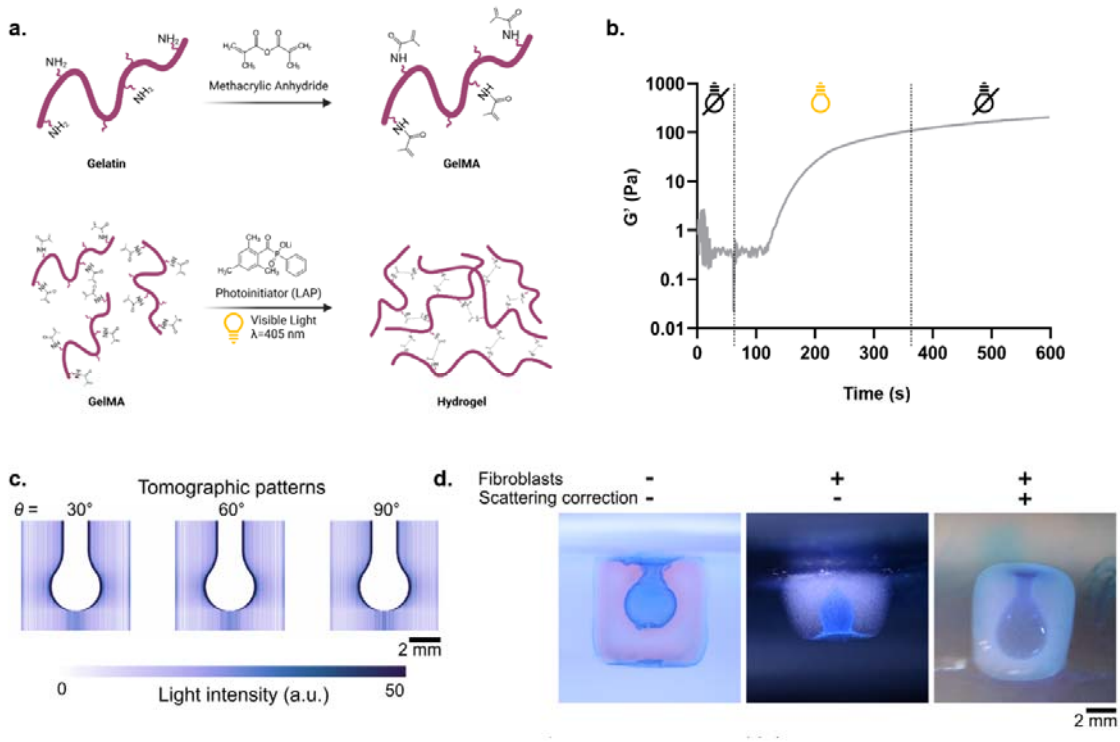

Fig. 2. Fabrication of viable 3D pancreatic ductal models. a. Synthesis and photocrosslinking of gelatin methacryloyl (GelMA) inspired from Yoon et al.[57]. Gelatin was reacted with methacrylic anhydride (MA) to introduce a methacryloyl substitution group on the reactive amine and hydroxyl groups of the amino acid residues. The GelMA photocrosslinking occurs after exposure to visible light (405 nm wavelength). The free radicals generated by the photoinitiator initiate the chain polymerization with methacryloyl substitution resulting in the hydrogel formation. **b.** Photorheology test to evaluate the photocrosslinking kinetic by monitoring the storage modulus (G') overtime. The crosslinking reaction started after 60 s following the emission of visible light (405 nm wavelength). **c.** Some tomographic patterns used to fabricate the scattering-corrected constructs. In total, 1000 different tomographic patterns are displayed along each turn of the cylindrical vial during printing. **d.** Photographs of 3D printed GelMA constructs, immersed in water and with the duct filled with a glycerol-based blue dye for illustrative purposes. Including cells in the gel affects print fidelity, but it can be compensated by correcting for scattering effects.

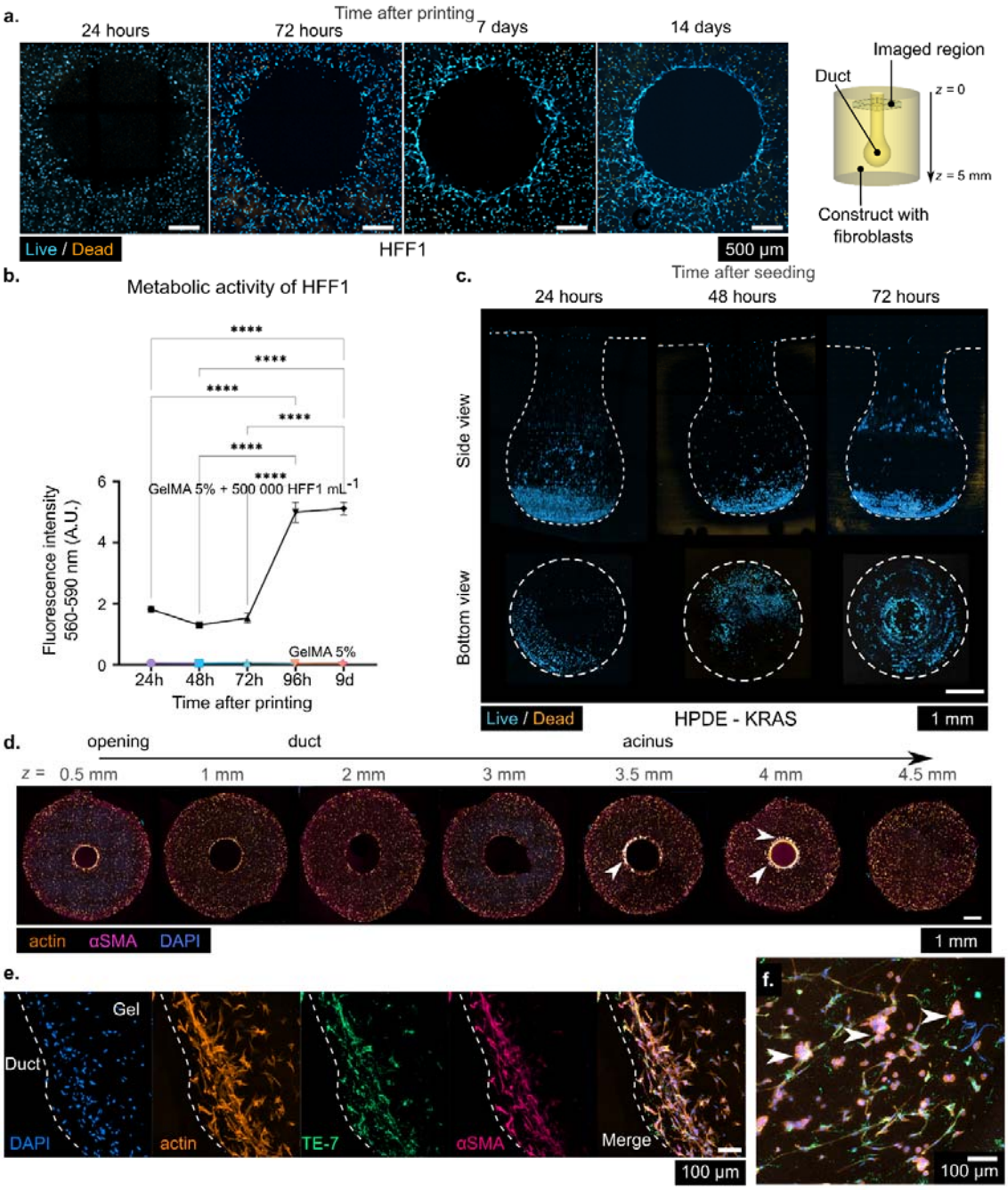

Fig. 3. Viability of pancreatic ductal models. a. Live/Dead assay of fibroblasts performed on different samples 1, 3, 7 and 14 days after volumetric bioprinting. A schematic shows the region where these microscopy images were acquired. **b.** Metabolic activity of fibroblasts (black) as a function of time, measured from the reduction of resazurin. Cell-free printed hydrogels (color) are used as a control (nGelMA + cells = 7, nGelMa = 7). Tukey's multiple comparisons test: *$p < 0.05$, **$p < 0.01$, ***$p < 0.001$, ****$p < 0.0001$. Error bars represent one standard deviation. **c.** Injected HPDE cells progress over time to line the inner face of the 3D bioprinted pancreatic model duct. **d.** Immunofluorescence micrographs of seven 300 µm thick slices of a 3D bioprinted pancreatic model taken 72 hours after HPDE-KRAS cells seeding and 5 days after bioprinting process. White arrows highlight migration of HPDE-KRAS cells inside the fibroblast-laden hydrogel. **e.** High-magnification multi-channel fluorescence microscopy images of the duct wall of a fibroblast-laden construct co-

cultured with HPDE-KRAS cells. Fibroblasts take long shapes. **f.** HPDE cells, shown with arrows, form grape-like clusters of smaller round cells (color scheme is the same as *e*).

3.3 Evaluation of cell-cell crosstalk within the pancreatic *in vitro* model

We studied the effect of crosstalk between HPDE cells and HFF1 evaluating changes in the cytoskeleton composition of the latter. In particular, healthy HPDE (HPDE-WT) and HPDE overexpressing the KRAS mutation (HPDE-KRAS) were seeded in the fibroblast-laden hydrogels 4 days after the bioprinting process. We exploited the HFF1 recovery occurring during the first 96h, when the viability significantly increased, to implement the co-culture conditions. Immunofluorescence microscopy was performed on 300 μm thick transversal slices of HFF1-laden constructs containing HPDE-WT cells, HPDE-KRAS, and without HPDE cells as a control (n = 4 replicas for HPDE-WT 72 hours; n = 3 for all other treatments) at 5 and 7 days after printing (24 and 72 hours after HPDE seeding), as seen in Fig. 4a. We used thin slices of the gel obtained with a vibratome to guarantee that antibodies would penetrate evenly throughout the constructs and that all cells in them could be imaged. Anti-αSMA antibody, phalloidin-FITC (an actin marker), and DAPI (a DNA marker) were used to identify cells morphology and to evaluate the appearance of a myofibroblast phenotype associated with an increased expression of αSMA. Qualitatively, we see that fibroblasts in constructs seeded with HPDE-KRAS cells exhibit stronger expression of αSMA, and that this expression increases with time. We developed an algorithm to automatically and blindly quantify the expression of αSMA with respect to actin over hundreds of cells in several complete slices of the constructs, which were imaged under a confocal microscope following a standardized protocol. The automated analysis used the DAPI signal to detect cells, from which it would then compute the ratio of the intensities of αSMA vs. actin, a proxy of fibroblast activation, as shown in Fig. 4b. This analysis shows that the mean fibroblast activation increases after exposure to HPDE-KRAS, but not so after exposure to the non-cancerous HPDE-WT. The level of fibroblast activation is also significantly higher after being in co-culture with HPDE-KRAS for 72 hours compared to 24 hours (p = 0.018). We also studied the dependence of fibroblast activation with the distance to the duct at the single cell level. Fig. 4c shows these measurements, suggesting an increased activation for fibroblasts closer to the duct, where HPDE-KRAS cells lay. In contrast, fibroblasts co-cultured with HPDE-WT cells or with no HPDE cells did not exhibit a decaying degree of activation with distance to the duct. These results indicate that the activation of fibroblasts occurs predominantly when they are co-cultured with HPDE-KRAS cells and that the dependence of αSMA expression on the distance from the duct is evident only in this condition.

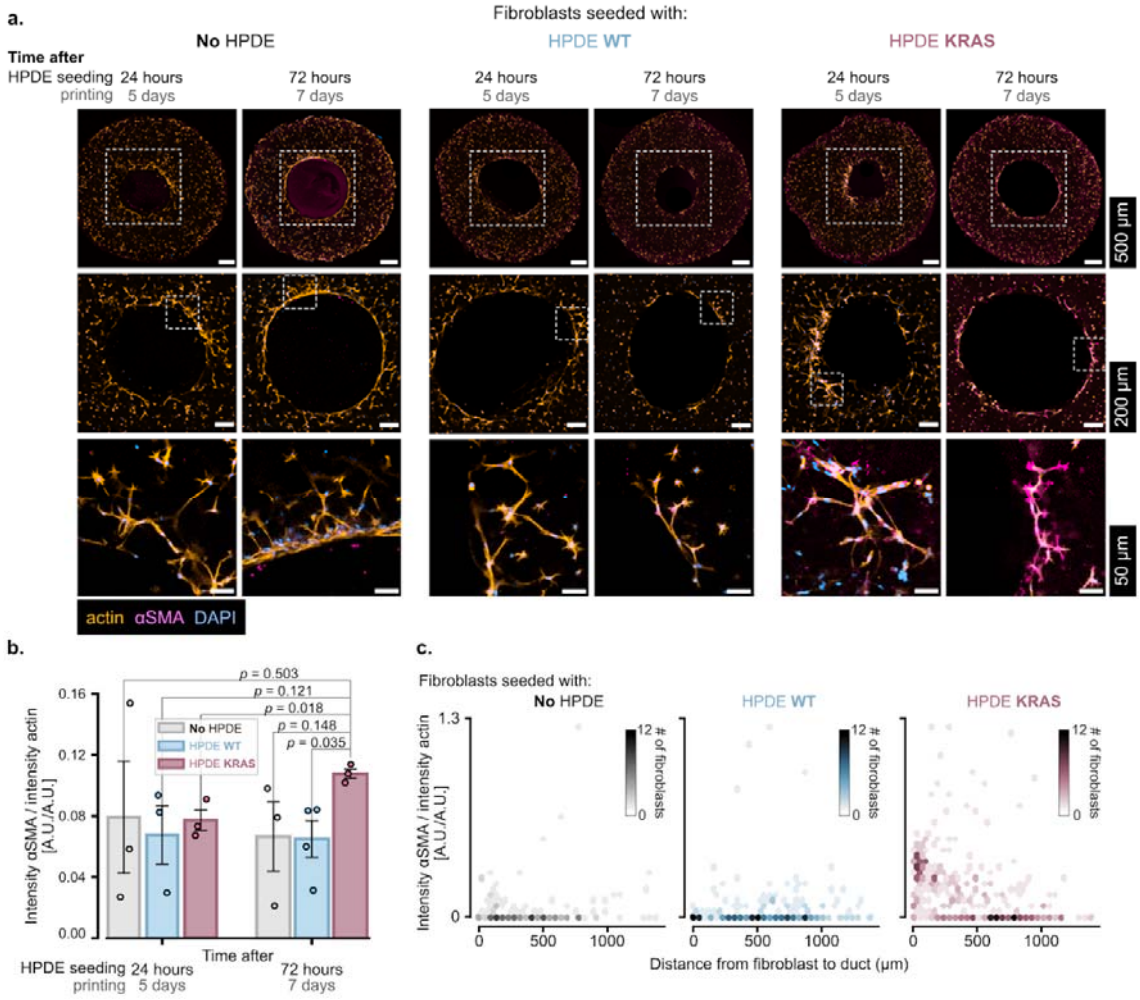

Fig. 4. Tomographic biofabricated 3D pancreatic models recapitulate inflammation of cancer-associated fibroblasts. a. Fluorescence microscopy images of full slices of constructs without HPDE cells and seeded with HPDE-WT or HPDE-KRAS cells 24 hours (5 days) and 72 hours (7 days) after bioprinting. Lower rows correspond to close-ups of the dashed regions. Scale bars top row: 500 µm, mid row: 200 µm, bottom row: 50 µm. **b.** Ratio of fluorescence intensity of **α**SMA vs. actin. (*n = 4* for HPDE-WT 72 hours after seeding, *n = 3* for all other treatments). Error bars indicate standard error of the mean. *p*-values come from one-way ANOVA tests. **c.** Density maps of the ratio of **α**SMA intensity over actin intensity in individual fibroblasts vs. distance from the cell to the edge of the duct. Data come from samples 7 days after printing (72 hours after seeding). Number of fibroblasts: $n_{No\ HPDE}$ = 143, $n_{HPDE\ WT}$ = 231, $n_{HPDE\ KRAS}$ = 350.

4. Discussion

Despite several efforts focused on the investigation of pancreatic cancer progression over the past decades, pancreatic ductal adenocarcinoma (PDAC) remains one of the most lethal tumors, with the highest 1-year, 5-year and 10-year mortalities of any cancer type[3]. Modelling the dynamic phenomena involved in tumor-stroma interplay is essential to not only increase the knowledge of the disease but also experiment with new and more effective

treatments to cure it. Indeed, the stromal tissue surrounding the PDAC site represents a histopathological hallmark of pancreatic cancer[58–63] and plays a fundamental role in tumor progression[64,65].

In this study we developed a 3D *in vitro* model of the exocrine pancreas which mimics the compartmentalized architecture of the native tissue and allows to recapitulate the stromal and pancreatic cancer cells crosstalk on the same miniaturized construct. We co-cultured human fibroblasts to model the stromal component and human pancreatic epithelial cells, healthy or expressing the KRAS oncogene, to reproduce the exocrine pancreatic tissue, respectively normal or pathological (Fig. 1).

To microfabricate the acinar- and ductal-like geometry, typical of the functional unit of the exocrine pancreas, tomographic volumetric bioprinting was adopted. This one-step, cell-friendly and scalable approach guaranteed high shape fidelity allowing to obtain in a few minutes a 3D cell-laden hydrogel incorporating a cavity, which is constituted of a duct converging to an enlarged lumen (acinus) (Fig. 2).

We demonstrated the printing of relevant object shape for biological studies while maintaining a suitable environment for the growth of stromal cells (HFF1) that remain viable and active for at least 2 weeks after the manufacturing process (Fig. 3a,b). This is in line with other works, which have cultured viable tomographically printed constructs for several weeks[46,51,66]. Therefore, the results proved the beneficial effects given by GelMA as bioink, matching with previous reports on the extensive use of this material in biomedical applications[67–71]. Moreover, by exploiting VBP features, the complex hollow structure of the exocrine pancreas can be fabricated without the use of a mould and without the need for sacrificial or support materials as opposed to more conventional (bio)printing and additive manufacturing methods that typically build 3D objects in a layer-by-layer fashion[72]. This innovative biofabrication approach also avoids the technical difficulties and time-consuming procedures associated with the assembling of different cellularized compartments into a unique 3D structure[42].

The cavity within the printed construct constitutes a biomimetic niche which can be easily epithelized by seeding the human pancreatic ductal epithelial cells, suspended in a proper volume of cell medium. We monitored the proliferation of HPDE cells over time and we assessed their ability to cover the inner walls of the lumen by growing as an epithelial monolayer, as already reported by other studies in literature[43,73]. However, the total coverage of the cavity has not been achieved (Fig. 3c) during the experiment period (3 days) and we observed a slower proliferation rate of HPDE seeded in fibroblast-laden hydrogels with respect to cell-free GelMA constructs (sup. fig. 2a). This behavior could be ascribed to the competition for nutrients in cell medium by both the cell lines[74] reducing cell proliferation without affecting cell viability (sup. fig. 2b).

Under co-culture conditions we monitored the activation of stromal cells by quantifying, through a custom-made Python code, the signal intensity coming from the expression of SMA proteins (Fig. 4). The results, showing a higher SMA expression in fibroblasts co-cultured with HPDE-KRAS rather than in contact with HPDE-WT, allow to validate this *in vitro* model as it can efficiently replicate the physiological inflammation cascade occurring in activated stromal cells[29,33,34,75].

Moreover, the developed model is the first to recapitulate the tumor-stroma interplay occurring in pancreatic cancer while also accurately reproducing the anatomical structure of the exocrine gland. The geometrical and morphological features of a tissue can affect the cell functionality and therefore represent another crucial aspect to consider in the design of a biomimetic model[41,76]. Although different engineering strategies have been adopted to obtain tubular lumen structures[41–43,73,77], they lack in fully creating the 3D acinar- and ductal-like geometry[42,73] or in incorporating the stromal component[43,78]. However, our model currently replicates the glandular structure with 5:1 rescaled dimensions as compared to the physiological human gland (diameter of acinar portion 200 µm, of duct portion 50 µm). This ratio is comparable or smaller than that of other models replicating the morphology of the pancreactic gland, including a hollow duct[43]. Additional work should be performed to enhance the resolution of the printed cavity, to make it more anatomically relevant[78]. In this context, the methodology applied to produce the *in vitro* model allows for a highly versatile approch, therefore, this model could be further improved by incorporating other cells involved in pathology development. For instance, tissue-resident immune cells could be included inside the construct to assess the role of immune system in the early stages of pancreatic cancer progression.

Finally, this model recapitulating the tumor-associated fibroblasts activation could open new avenues to understand the role of tumor microenvironment in pancreatic cancer progression and offers a new and relevant platform to establish effective therapeutical strategies. Our approach permits to overcome the limitations of the existing *in vitro* models that do not properly mimic the morphology, the cell composition and the cell-stroma interplay of the exocrine pancreas environment. In addition, it represents a valid alternative to the costly and low-throughput animal models which are ethically questionable and limited in emulating the stromal components of PDAC[79,80]. Indeed, the rapid fabrication process allows to obtain several scalable human models that can be tested and validated according to a high throughput screening approach.

5. Conclusions

In this study, we have developed a 3D *in vitro* model which mimics the complex three-dimensional microanatomy of the exocrine pancreas to study the mechanisms that take place during the early stages of pancreatic cancer. We used VBP, a recently-developed and powerful printing technique, to fabricate acinar- and ductal-like structures. We showed that this biofabrication approach allows the series production of several human models with shape-fidelity, high resolution and geometrical accuracy. The GelMA-based environment resulted optimal in promoting the proliferation of stromal cells which remain viable and active for several weeks within the gel structure thus permitting a long follow-up.
The co-culture of human pancreatic ductal epithelial cells, healthy or overexpressing the KRAS oncogene, and stromal cells in this biofabricated *in vitro* model can recapitulate the pancreatic TME as confirmed by the stromal cells' activation through the tumor-stroma crosstalk. In particular, we demonstrated the ability of this model in reproducing the stromal cells activation, involved in pancreatic cancer evolution, in a very short period (3 days under co-colture and 7 days after biofabrication). Moreover, the construct can be monitored over time in an accessible and non-destructive way by microscopy to quantitively interrogate the

model and easily get the information. These results validate our approach that is scalable and therefore potentially applicable in a personalized medicine workflow, in which the patients' own cells are used to build many models of the exocrine pancreas' microanatomy in a short period of time to rapidly adjust the therapy to the patient. This could enhance treatment outcomes and reduce healthcare costs. Thus, the demonstration of this fully human 3D model represents a powerful tool for the understanding of mechanisms implicated in pancreatic cancer insurgence and for developing new diagnostic and therapeutical approaches.

6. Methods

GelMA Hydrogels

GelMA was produced from porcine gelatin (Sigma) following the protocol by Van De Bulcke *et al.*[81]. Briefly, type A porcine gelatin powder (Sigma, G2500) was fully dissolved at 10% w/v into Phosphate Buffered Saline (PBS) 1x at 50 °C. Methacrylic anhydride (Sigma, 760-93-0) was added dropwise for gelatin modification at 50 °C for 3 h. The solution was then lyophilized and stored away from light at −20 °C until use. The 5% w/v GelMA solution was created by reconstituting lyophilized GelMA powder into sterile DMEM without phenol red (ThermoFisher, 31053028) with Lithium phenyl-2,4,6-trimethylbenzoylphosphinate (LAP, Sigma-Aldrich, 900889) at a concentration of 0.16 mg mL^{-1} and filter-sterilized at 40°C. GelMA solutions were stored away from ambient light at 4 °C for no longer than 2 weeks. Before use, the rheological properties of GelMA hydrogels were evaluated employing a stress-controlled rheometer (AntonPaar GmbH, MCR302) equipped with 25 mm parallel plate geometry. In order to evaluate the photocrosslinking kinetics, filtered GelMA solution + LAP were poured on the rheometer plate and time sweep test was performed using a visible light source at 405 nm wavelength (Prizmatix, FC-LED-405A) at constant temperature (approximately 25 °C), a applying a rotational oscillation of 1 Hz and a strain amplitude of 1% in the linear viscoelastic region (measured through strain sweep test).

Cell culture of HFF1

Human foreskin fibroblasts (HFF1) cells were purchased from ATCC® and cultured in Dulbecco's Modified Eagle's Medium (DMEM) without phenol red, supplemented with 1% Penicillin-Streptomycin (Gibco), 2% L-glutamine (Gibco) and 15% FBS (Gibco). Cells were maintained in a humidified CO_2 incubator at 37 °C and 5% CO_2.

Tomographic bioprinting

For printing, fibroblasts were detached, counted, and centrifuged. A small volume of cells, corresponding to a final density of 0.5 million cells mL^{-1}, was resuspended into GelMA with LAP and gently agitated using a 1000 µL pipette tip with a cut tip. 1.5 mL of the GelMA + LAP + HFF1 mix was poured into ethanol sterilized cylindrical glass vials (diameter 12 mm) with a hermetically sealing cap. All these manipulations were carried out under sterile conditions in a biosafety cabinet.

The glass flasks were dipped into water at 2°C to gelify the GelMA. They were then printed using a tomographic volumetric printer[46]. In this printer, blue light from three 405 nm laser diodes (Ushio, HL40033G) is sent through a square-core multi-mode optical fiber (CeramOptec, WF 70×70/115/200/400N), expanded, and projected on a Digital Micromirror

Device (mirror size=13.7 μm, Vialux, VIS-7001), which displays the tomographic patterns. Two plano-convex lenses with focal length f_1 = 150 mm and f_2 = 250 mm project the images from the DMD onto the rotating vial. The vial is set to rotate using a high-precision stage (Zaber, X-RSW60C), and is inside a cubic glass container filled with cold water, acting as a refractive-index matching bath.

The calculations to produce the required tomographic patterns were performed using the software described in a previous work[47], and scattering corrections were applied to compensate for the diffusive effects of the cell-laden hydrogels. These calculations were performed on a GPU using PyTorch[82]. This software takes 3D models in the shape of .stl files, which we designed using AutoCAD, and calculates tomographic projections using non-negative tomographic filtered back-projections. We used sets of 1000 8-bit tomographic patterns, each displayed for an angular interval of $\Delta\theta$ = 0.36°. The cylindrical vials were set to rotate at a constant angular speed of 12°/s during printing. Prints were completed in around 2.5 minutes.

After printing, glass vials were slowly heated to 27°C for 5 minutes by dipping them into water. Under sterile conditions in a biosafety cabinet, pre-warmed PBS at 37°C was gently pipetted into the glass vials, then they were gently manually agitated to rinse away the uncross-linked GelMA. The rinsed bioprinted fibroblast-laden constructs were carefully transferred to 24-well plates filled with cell medium and kept in the humidified CO_2 incubator at 37°C.

Cell viability in bioprinted constructs

CellTiter-Blue Viability Assay

The viability of human fibroblasts embedded in the bioprinted gel constructs was analyzed by monitoring the metabolic activity through the fluorimetric resazurin reduction method (CellTiter-Blue, Promega, G8080) at 1, 2, 3, 4 and 9 days after the tomographic bioprinting process. The test was performed according to the manufacturers' protocols. Briefly, culture medium was carefully removed and constructs were washed with PBS (500 μL). A solution of 16% CellTiter-Blue in complete cell culture medium was prepared and added to the constructs, followed by 5-6 h incubation at 37 °C. At the end of the incubation period, 200 μL of the medium was pipetted into different wells of a 96-well plate, and fluorescence was measured from the bottom of the plate using a plate reader (BioTek) at 530 nm excitation and 590 nm emission. Fluorescence of CellTiter-Blue solutions in contact with GelMA hydrogels without cells were subtracted to avoid overestimations. Plates were covered with an adhesive film to prevent evaporation during the measurements.

Live/Dead Assay

Live/Dead Assay was carried out to furtherly evaluate the HFF1 viability over the culture period, at pre-determined time points (1, 3, 7 and 14 days). Specifically, the Live/Dead solution was prepared by adding ethidium homodimer-1 (Adipogen, CDX-E0512-M001, 2mM in DMSO) and calcein-AM (Merck, 206700-1MG, resuspended to 4mM in DMSO) to PBS in concentrations of 4 μM and 2 μM respectively. The solution, prepared afresh every time it was used, was vortex-agitated for some seconds and kept at room temperature (RT) protected from light. The cellularized constructs were rinsed once with pre-warmed PBS at 37°C and transferred to a 24-well plate with wells filled with 800 μL of Live/Dead solution.

Constructs were incubated in the dark for 1h, with gentle manual agitation every 15 minutes. Samples were rinsed twice with PBS and placed in optical-grade multiwell microscope slides for imaging. Imaging was conducted immediately after staining and performed in a fluorescence confocal inverted microscope (Leica, SP8) with 5x NA 0.15 (Leica, HC PL Fluotar, WD 13.7 mm), 10x NA 0.30 (Leica, HC PL Fluotar, WD 11.0 mm), and 20x NA 0.75 (Leica, HC PL APO, WD 0.62 mm) objectives. In the microscope, calcein-AM was excited at 488 nm and its emission collected from 498 to 542 nm. Ethidium homodimer was excited at 552 nm. To avoid crosstalk with the emission spectrum of calcein-AM, the emission of Ethidium was collected from 620 nm to 650 nm.

Epithelization of the cavity

Human pancreatic ductal epithelial cells (HPDE) stably expressing activated KRAS (HPDE-KRAS) and wild-type HPDE (HPDE-WT) were cultured in RPMI-1640 medium (Gibco, Thermo Fisher Scientific) supplemented with 1% Penicillin-Streptomycin (Gibco), 1% L-glutamine (Gibco) and 10% fetal bovine serum (FBS) (Gibco). Cells were maintained in a humidified CO_2 incubator at 37 °C and 5% CO_2.

To epithelize the constructs, HPDE cells were detached from the culture flask, counted and resuspended to a 10 µL volume. Then, they were gently manually injected with micropipette into the duct of the fibroblast-laden hydrogel. Specifically, before the epithelization, the rinsed bioprinted fibroblast-laden constructs were cultured for 96h.

The cell ratio between HPDE cells and HFF1 was fixed at 1:3, In accordance with studies reporting the relevancy that ratios of 1:1 to 1:3 have *in vivo*[83–85]. After injection, the constructs were placed in 24-well plates, with enough cell medium to keep them hydrated, but not enough to cover the entry of the lumen, to prevent HPDE cells from floating into the media. Co-cultures were maintained in DMEM/F-12 supplemented with 15% FBS (Gibco), 1% Penicillin-Streptomycin (Gibco) and 2% L-glutamine (Gibco) since previous tests demonstrated the efficacy of this culture medium composition in promoting the cell viability[86]. Two hours later, more medium was added to the wells, this time covering the full constructs. The constructs were maintained in a humidified CO_2 incubator at 37 °C and 5% CO_2.

Immunofluorescence microscopy

Slicing constructs for immunostaining

Bioprinted constructs were fixed in formaldehyde 4% v/v in PBS for 5 minutes, then rinsed with PBS twice and kept at 4°C. The fixed constructs were embedded in low-melting point agarose 4% w/v in pre-warmed PBS and sliced to a thickness of 300 µm with a vibratome (Leica Biosystems, VT1000S) filled with PBS 1x. Samples were sliced orthogonally to the axis of the duct, in order to obtain circular cross-sections. After slicing, the surrounding agarose was detached gently with a brush. Slices were put onto microscope slides with adhesive imaging spacers making wells (Merck, GBL654004-100EA), covered with PBS and with a coverslip and kept at 4°C in a dark wet chamber until they were stained for imaging

Immunostaining

Samples were permeabilized with 0.1% Triton X-100 in PBS for 10 minutes at RT, then washed 3 times for 5 minutes with PBS + 0.1% Triton X-100 (PBST) at RT. Then, samples

were blocked with 2% bovine serum albumin (BSA) in PBST for 60 minutes and rinsed once with PBS. Primary antibodies, rabbit polyclonal to alpha smooth muscle actin (Abcam, ab5694-100ug, 1:50), and mouse monoclonal fibroblasts antibody TE-7 (Novus Biologicals, NBP2-50082, 1:80) in PBST + 1% BSA were incubated for 36h at 4°C. Samples were then rinsed 3 times with PBST at RT for 5 minutes. The secondary antibodies, donkey anti-rabbit IgG + Alexa 647 (Thermofischer, A-31573) and donkey anti-Mouse IgG + Alexa 568 (Thermofischer, A10037), were incubated at a concentration of 1:200 in PBST + 1% BSA for 2h at RT. Samples were rinsed with PBST for 5 minutes at RT 3 times. ((R)-4-Hydroxy-4-methyl-Orn(FITC)□)-Phalloidin (1:60, 0.16 nmol mL^{-1}) was incubated in PBST + 1% BSA for 30 minutes at RT. Samples were rinsed with PBS for 5 minutes at RT 3 times. Samples were then stained with DAPI in PBS (1:1000) for 5 minutes at RT, washed once with PBS, and finally covered with coverslips for imaging. Samples were kept in wet chambers and protected from intense light during all the immunostaining protocol.

Confocal Microscopy

Samples were imaged with a motorized inverted confocal microscope (Leica SP8) using a 10x NA 0.30 air objective (WD = 11.0 mm, HC PL Fluorotar, Leica). Fluorescence excitation was performed with solid-state lasers at 405, 488, 552, and 638 nm, and its emission was collected with two twin Hybrid Detectors. An additional photomultiplier tube collected transmitted light from the excitation laser. To acquire images of the full cross sections of the bioprinted constructs, the automatic motorized stage was used to take sequential images along grids that were later stitched together. Two sequential two-channel acquisitions were performed for each sample; one collecting the fluorescence from DAPI (440-480 nm) and TE-7-bound secondary antibody (568-620 nm), and another collecting the fluorescence from Phalloidin-FITC (498-542 nm) and □SMA-bound secondary antibody (648-720 nm). Both acquisitions used the same grid coordinates of the motorized stage and included a bright field image acquisition. Lasers intensities, detector gain, and optical path were kept unchanged across image acquisitions to guarantee intensities were comparable. Microscopy images were automatically acquired using LAS X software (Leica). Images were acquired for almost 100 slices of 14 independent biological samples.

Image processing

Due to the large area of the acquired microscopy images (> 250 mm^2 in some cases) and to the fact that we were imaging soft, elastic hydrogels, there was displacement between the DAPI-TE-7 and the Phalloidin-□SMA images for some samples (note however, that because Phalloidin and □SMA were always acquired in parallel and not sequentially, there was never displacement between these two channels).

Displacement between the DAPI-Te-7 and Phalloidin-□SMA images was corrected with a custom-made Python code. The code compared the bright-field channels of corresponding DAPI-Te-7-BF and Phalloidin-□SMA-BF tiles, calculated the necessary homography ($n_{features}$ = 5000) that needed to be applied to the DAPI-Te-7-BF image so that it matched the Phalloidin-□SMA-BF image[87]. The code would then apply such homography and save a transformed copy of DAPI-Te-7-BF image.

Images were batch-stitched together using the Grid/Collection stitching plugin[88] on ImageJ[89] using the Phalloidin channel as reference. Multichannel microscopy images (DAPI,

Phalloidin, Te-7, SMA, BF) depicting multiple slices of the same bioprinted construct were then manually cropped to fit only one slice per image.

Inflammation quantification from fluorescence data

Inflammation was quantified from microscopy images by measuring the ratio between the intensity of SMA vs. actin. This calculation was done with a custom-made Python code. The code first segments cell nuclei from the DAPI channel. Then, the code segments all regions of at least 13.4 μm^2 with a non-zero actin or SMA intensity in size and which are adjacent to a cell nucleus. An average intensity is calculated for these masked regions for the actin and SMA channels, and a ratio is reported. Actin and SMA intensities were additionally normalized to excitation light intensities, to make the ratio comparable across multiple acquisitions.

Single-cell measurements of inflammation

The ratio of actin to SMA intensities was also computed for segmented single cells. Hand-made digital annotations of the outline of the inner channel of the bioprinted pancreatic constructs (based on the bright field and fluorescence channels of the microscopy images) were used to measure the distance of the individual cells to the channel.

Visualization of microscopy images

Multi-channel microscopy images were visualized using ImageJ and the Look-Up Tables from Christophe Leterrier (https://github.com/cleterrier/ChrisLUTs) for the Live/Dead experiments and from the BioImaging and Optics Platform at EPFL (https://biop.epfl.ch/Fiji-Update/luts/) for the co-culture inflammation experiments. Brightness and contrast were set the same for each channel of all images that were compared (particularly actin and αSMA). Sketches of cell-laden constructs were created with BioRender.com. Plots were produced using matplotlib.org[90] and seaborn.pydata.org[91].

Statistical analysis

Data were arranged and analyzed using Pandas[92]. The graph data are presented as the mean ± standard deviation (SD) for at least three independent experiments ($n \geq 3$). Significance was measured with one-way ANOVA followed by pairwise comparison with Tukey's multiple comparisons test, using GraphPad Prism 9.3.1 for metabolic activity experiment (*$p < 0.05$, **$p < 0.01$, ***$p < 0.001$, ****$p < 0.0001$) and using SciPy's statsmodels (https://www.statsmodels.org/stable/index.html) for inflammation quantification.

Data availability

All data from this work and the code used to process and analyze microscopy data and perform statistical analysis are freely available from the Zenodo repository 10.5281/zenodo.7525930.

Acknowledgements

We thank Dr. Lely Feletti and Prof. Aleksandra Radenovic from the Laboratory of Nanoscale Biology at EPFL for their support with cell culture and for sharing cell-culture equipment. We also thank Estée Grandidier for support with cell culture. Authors thank Dr. Jessica Sordet-

Dessimoz from EPFL's Histology Core Facility for useful discussions on immunostaining and Dr. Nicolas Chiaruttini for support with fluorescence microscopy. We also acknowledge Ragunathan Bava Ganesh from the Laboratory of Biological Network Characterization at EPFL for his support with fluorometry. We also thank Cecilia Traldi and Matteo Bortolameazzi for their support with the material characterization. The authors thank the open-source tools (and their contributors) which were used in this work, including FreeCADweb.org, Inkscape.org, Python.org, PyTorch.org, Pandas.Pydata.org, and Fiji.sc.

Funding: JMW, AB, and CM received funding from the European Union's Horizon 2020 research and innovation programme under grant agreement No 964497, and by the Swiss National Science Foundation under project number 196971 - "Light based Volumetric printing in scattering resins.

Conflicts of interest: CM is a shareholder of Readily3D SA. JMW, AB, and CM have filed provisional patent No. WO2022EP63245 20220517 regarding three-dimensional printing in complex media.

References

1. Khomiak A, Brunner M, Kordes M, et al. Recent Discoveries of Diagnostic, Prognostic and Predictive Biomarkers for Pancreatic Cancer. *Cancers (Basel)* 2020; 12: 3234.

2. Siegel RL, Miller KD, Jemal A. Cancer statistics, 2020. *CA Cancer J Clin* 2020; 70: 7–30.

3. Siegel RL, Miller KD, Fuchs HE, et al. Cancer statistics, 2022. *CA Cancer J Clin* 2022; 72: 7–33.

4. Orth M, Metzger P, Gerum S, et al. Pancreatic ductal adenocarcinoma: Biological hallmarks, current status, and future perspectives of combined modality treatment approaches. *Radiation Oncology* 2019; 14: 1–20.

5. Porciuncula A, Hajdu C, David G. The Dual Role of Senescence in Pancreatic Ductal Adenocarcinoma. *Adv Cancer Res* 2016; 131: 1–20.

6. Brunet LR, Hagemann T, Andrew G, et al. Have lessons from past failures brought us closer to the success of immunotherapy in metastatic pancreatic cancer? *Oncoimmunology*; 5. Epub ahead of print 2 April 2016. DOI: 10.1080/2162402X.2015.1112942.

7. Heinrich MA, Mostafa AMRH, Morton JP, et al. Translating complexity and heterogeneity of pancreatic tumor: 3D in vitro to in vivo models. *Adv Drug Deliv Rev* 2021; 174: 265–293.

8. Geyer M, Queiroz K. Microfluidic Platforms for High-Throughput Pancreatic Ductal Adenocarcinoma Organoid Culture and Drug Screening. *Front Cell Dev Biol* 2021; 9: 1–9.

9. Weniger M, Honselmann KC, Liss AS. The extracellular matrix and pancreatic cancer: A complex relationship. *Cancers*; 10. Epub ahead of print 6 September 2018. DOI: 10.3390/cancers10090316.

10. Fu Y, Liu S, Zeng S, et al. The critical roles of activated stellate cells-mediated paracrine signaling, metabolism and onco-immunology in pancreatic ductal adenocarcinoma. *Molecular Cancer*; 17. Epub ahead of print 19 February 2018. DOI: 10.1186/s12943-018-0815-z.

11. Liang T, Dolai S, Xie L, et al. Ex vivo human pancreatic slice preparations offer a valuable model for studying pancreatic exocrine biology. *J Biol Chem* 2017; 292: 5957.

12. Hidalgo M, Cascinu S, Kleeff J, et al. Addressing the challenges of pancreatic cancer: Future directions for improving outcomes. *Pancreatology* 2015; 15: 8–18.

13. Liot S, Balas J, Aubert A, et al. Stroma Involvement in Pancreatic Ductal Adenocarcinoma: An Overview Focusing on Extracellular Matrix Proteins. *Frontiers in Immunology* 2021; 12: 709.

14. Wang S, Li Y, Xing C, et al. Tumor microenvironment in chemoresistance, metastasis and immunotherapy of pancreatic cancer. *Am J Cancer Res* 2020; 10: 1937.

15. Apte M V., Wilson JS, Lugea A, et al. A starring role for stellate cells in the pancreatic cancer microenvironment. *Gastroenterology* 2013; 144: 1210–1219.

16. Monteiro M V, Ferreira LP, Rocha M, et al. Journal Pre-proof Advances in bioengineering pancreatic tumor-stroma physiomimetic Biomodels. *Biomaterials*. Epub ahead of print 2022. DOI: 10.1016/j.biomaterials.2022.121653.

17. Zhan H-X, Zhou B, Cheng Y-G, et al. Crosstalk between stromal cells and cancer cells in pancreatic cancer: New insights into stromal biology. *Cancer Lett* 2017; 392: 83–93.

18. Bynigeri RR, Jakkampudi A, Jangala R, et al. Pancreatic stellate cell: Pandora's box for pancreatic disease biology. *World J Gastroenterol* 2017; 23: 382.

19. Nielsen MFB, Mortensen MB, Detlefsen S. Key players in pancreatic cancer-stroma interaction: Cancer-associated fibroblasts, endothelial and inflammatory cells. *World Journal of Gastroenterology* 2016; 22: 2678–2700.

20. Hruban RH, Adsay NV, Albores-Saavedra J, et al. Pathology of genetically engineered mouse models of pancreatic exocrine cancer: Consensus report and recommendations. *Cancer Res* 2006; 66: 95–106.

21. Chari ST. Detecting Early Pancreatic Cancer: Problems and Prospects. *Semin Oncol* 2007; 34: 284–294.

22. Cui SJ, Tang TY, Zou XW, et al. Role of imaging biomarkers for prognostic prediction in patients with pancreatic ductal adenocarcinoma. *Clin Radiol*. Epub ahead of print 2020. DOI: 10.1016/j.crad.2019.12.023.

23. Cave DD, Rizzo R, Sainz B, et al. The revolutionary roads to study cell–cell interactions in 3d in vitro pancreatic cancer models. *Cancers (Basel)* 2021; 13: 1–19.

24. Osuna de la Peña D, Trabulo SMD, Collin E, et al. Bioengineered 3D models of human pancreatic cancer recapitulate in vivo tumour biology. *Nat Commun 2021 121* 2021; 12: 1–15.

25. Haque MR, Rempert TH, Al-Hilal TA, et al. Organ-Chip Models: Opportunities for

Precision Medicine in Pancreatic Cancer. *Cancers (Basel)* 2021; 13: 4487.

26. Mollica H, Teo YJ, Tan ASM, et al. A 3D pancreatic tumor model to study T cell infiltration. *Biomater Sci* 2021; 9: 7420–7431.

27. Schuster B, Junkin M, Kashaf SS, et al. Automated microfluidic platform for dynamic and combinatorial drug screening of tumor organoids. *Nat Commun* 2020; 11: 1–12.

28. Nguyen DHT, Lee E, Alimperti S, et al. A biomimetic pancreatic cancer on-chip reveals endothelial ablation via ALK7 signaling. *Sci Adv* 2019; 5: 1–10.

29. Monteiro M V., Rocha M, Gaspar VM, et al. Programmable Living Units for Emulating Pancreatic Tumor-Stroma Interplay. *Adv Healthc Mater* 2022; 2102574.

30. Wishart G, Gupta P, Schettino G, et al. 3d tissue models as tools for radiotherapy screening for pancreatic cancer 1,2. *Radiol* 2021; 94: 20201397.

31. Brancato V, Comunanza V, Imparato G, et al. Bioengineered tumoral microtissues recapitulate desmoplastic reaction of pancreatic cancer. *Acta Biomater* 2017; 49: 152–166.

32. Tomás-Bort E, Kieler M, Sharma S, et al. 3D approaches to model the tumor microenvironment of pancreatic cancer. *Issue 11 Theranostics* 2020; 10: 5074–5089.

33. Lazzari G, Nicolas V, Matsusaki M, et al. Multicellular spheroid based on a triple co-culture: A novel 3D model to mimic pancreatic tumor complexity. *Acta Biomater* 2018; 78: 296–307.

34. Lai BFL, Lu RXZ, Hu Y, et al. Recapitulating Pancreatic Tumor Microenvironment through Synergistic Use of Patient Organoids and Organ-on-a-Chip Vasculature. *Adv Funct Mater* 2020; 2000545: 1–16.

35. Yu Y, Yang G, Huang H, et al. Preclinical models of pancreatic ductal adenocarcinoma: challenges and opportunities in the era of precision medicine. *Journal of Experimental and Clinical Cancer Research* 2021; 40: 1–13.

36. Gündel B, Liu X, Löhr M, et al. Pancreatic Ductal Adenocarcinoma: Preclinical in vitro and ex vivo Models. *Front Cell Dev Biol* 2021; 9: 1–12.

37. Uzunparmak B, Sahin IH. Pancreatic cancer microenvironment: a current dilemma. *Clin Transl Med 2019 81* 2019; 8: 1–8.

38. Hingorani SR. Epithelial and stromal co-evolution and complicity in pancreatic cancer. DOI: 10.1038/s41568-022-00530-w.

39. Kota J, Hancock J, Kwon J, et al. Pancreatic cancer: Stroma and its current and emerging targeted therapies. *Cancer Lett* 2017; 391: 38–49.

40. Pothula SP, Pirola RC, Wilson JS, et al. Pancreatic stellate cells: Aiding and abetting pancreatic cancer progression. *Pancreatology* 2020; 20: 409–418.

41. Hajiabbas M, D'Agostino C, Simińska-Stanny J, et al. Bioengineering in salivary gland regeneration. *J Biomed Sci 2022 291* 2022; 29: 1–24.

42. Gupta P, Pérez-Mancera PA, Kocher H, et al. A Novel Scaffold-Based Hybrid Multicellular Model for Pancreatic Ductal Adenocarcinoma—Toward a Better Mimicry

of the in vivo Tumor Microenvironment. *Front Bioeng Biotechnol*; 8. Epub ahead of print 2020. DOI: 10.3389/fbioe.2020.00290.

43. Venis SM, Moon HR, Yang Y, et al. Engineering of a functional pancreatic acinus with reprogrammed cancer cells by induced: PTF1a expression. *Lab Chip* 2021; 21: 3675–3685.

44. Charbonneau AM, Kinsella JM, Tran SD. 3D cultures of salivary gland cells in native or gelled egg yolk plasma, combined with egg white and 3D-printing of gelled egg yolk plasma. *Materials (Basel)* 2019; 12: 1–16.

45. Jain P, Kathuria H, Dubey N. Advances in 3D bioprinting of tissues/organs for regenerative medicine and in-vitro models. *Biomaterials* 2022; 287: 121639.

46. Bernal PN, Bouwmeester M, Madrid-Wolff J, et al. Volumetric Bioprinting of Organoids and Optically Tuned Hydrogels to Build Liver-Like Metabolic Biofactories. *Adv Mater* 2022; 34: 2110054.

47. Madrid-Wolff J, Boniface A, Loterie D, et al. Controlling Light in Scattering Materials for Volumetric Additive Manufacturing. *Adv Sci* 2022; 9: 2105144.

48. Gehlen J, Qiu W, Müller R, et al. Volumetric Tomographic 3D Bioprinting of Heterocellular Bone- like Tissues in Seconds. 2021; 1–24.

49. Rizzo R, Ruetsche D, Liu H, et al. Optimized Photoclick (Bio)Resins for Fast Volumetric Bioprinting. *Adv Mater*; 33. Epub ahead of print 2021. DOI: 10.1002/adma.202102900.

50. Sola A, Bertacchini J, D'Avella D, et al. Development of solvent-casting particulate leaching (SCPL) polymer scaffolds as improved three-dimensional supports to mimic the bone marrow niche. *Mater Sci Eng C* 2019; 96: 153–165.

51. Bernal PN, Delrot P, Loterie D, et al. Volumetric Bioprinting of Complex Living-Tissue Constructs within Seconds. *Adv Mater* 2019; 31: 1904209.

52. Loterie D, Delrot P, Moser C. High-resolution tomographic volumetric additive manufacturing. *Nat Commun* 2020; 11: 1–6.

53. Kelly BE, Bhattacharya I, Heidari H, et al. Volumetric additive manufacturing via tomographic reconstruction. *Science (80-)* 2019; 363: 1075–1079.

54. Wex C, Fröhlich M, Brandstädter K, et al. Experimental analysis of the mechanical behavior of the viscoelastic porcine pancreas and preliminary case study on the human pancreas. *J Mech Behav Biomed Mater* 2015; 41: 199–207.

55. Kinstlinger IS, Saxton SH, Calderon GA, et al. Generation of model tissues with dendritic vascular networks via sacrificial laser-sintered carbohydrate templates. DOI: 10.1038/s41551-020-0566-1.

56. Lee GM, Kim S jeong, Kim EM, et al. Free radical-scavenging composite gelatin methacryloyl hydrogels for cell encapsulation. *Acta Biomater* 2022; 149: 96–110.

57. Yoon HJ, Shin SR, Cha JM, et al. Cold Water Fish Gelatin Methacryloyl Hydrogel for Tissue Engineering Application. *PLoS One* 2016; 11: e0163902.

58. Procacci P, Moscheni C, Sartori P, et al. Tumor–Stroma Cross-Talk in Human Pancreatic Ductal Adenocarcinoma: A Focus on the Effect of the Extracellular Matrix on Tumor Cell Phenotype and Invasive Potential. *Cells 2018, Vol 7, Page 158* 2018; 7: 158.

59. Matsuzawa A, Cortesi M, Zanoni M, et al. Pancreatic Cancer and Cellular Senescence: Tumor Microenvironment under the Spotlight. *Int J Mol Sci 2022, Vol 23, Page 254* 2021; 23: 254.

60. Thomas D, Radhakrishnan P. Tumor-stromal crosstalk in pancreatic cancer and tissue fibrosis. *Mol Cancer*; 18. Epub ahead of print 21 January 2019. DOI: 10.1186/S12943-018-0927-5.

61. Hadden M, Mittal A, Samra J, et al. Mechanically stressed cancer microenvironment: Role in pancreatic cancer progression. *Biochim Biophys Acta - Rev Cancer* 2020; 1874: 188418.

62. Gardian K, Janczewska S, Olszewski WL, et al. Analysis of Pancreatic Cancer Microenvironment: Role of Macrophage Infiltrates and Growth Factors Expression. *J Cancer* 2012; 3: 285.

63. Farrow B, Albo D, Berger DH. The Role of the Tumor Microenvironment in the Progression of Pancreatic Cancer. *J Surg Res* 2008; 149: 319–328.

64. Ho WJ, Jaffee EM, Zheng L. The tumour microenvironment in pancreatic cancer — clinical challenges and opportunities. *Nature Reviews Clinical Oncology* 2020; 17: 527–540.

65. Sperb N, Tsesmelis M, Wirth T. Crosstalk between tumor and stromal cells in pancreatic ductal adenocarcinoma. *International Journal of Molecular Sciences* 2020; 21: 1–23.

66. Ning L, Shim J, Tomov ML, et al. A 3D Bioprinted in vitro Model of Neuroblastoma Recapitulates Dynamic Tumor-Endothelial Cell Interactions Contributing to Solid Tumor Aggressive Behavior. *Adv Sci* 2022; 9: 2200244.

67. Colosi C, Shin SR, Manoharan V, et al. Microfluidic Bioprinting of Heterogeneous 3D Tissue Constructs Using Low-Viscosity Bioink. *Adv Mater* 2016; 28: 677-684a.

68. Kilic Bektas C, Hasirci V. Cell loaded 3D bioprinted GelMA hydrogels for corneal stroma engineering. *Biomater Sci* 2020; 8: 438–449.

69. Billiet T, Gevaert E, De Schryver T, et al. The 3D printing of gelatin methacrylamide cell-laden tissue-engineered constructs with high cell viability. *Biomaterials* 2014; 35: 49–62.

70. Klotz BJ, Gawlitta D, Rosenberg AJWP, et al. Gelatin-Methacryloyl Hydrogels: Towards Biofabrication-Based Tissue Repair. *Trends Biotechnol* 2016; 34: 394–407.

71. Alexa RL, Iovu H, Ghitman J, et al. 3D-printed gelatin methacryloyl-based scaffolds with potential application in tissue engineering. *Polymers (Basel)* 2021; 13: 1–17.

72. Moroni L, Boland T, Burdick JA, et al. Biofabrication: A Guide to Technology and Terminology. *Trends Biotechnol* 2018; 36: 384–402.

73. Moon HR, Ozcelikkale A, Yang Y, et al. An engineered pancreatic cancer model with intra-tumoral heterogeneity of driver mutations. *Lab Chip* 2020; 20: 3720–3732.

74. Freischel AR, Damaghi M, Cunningham JJ, et al. Frequency-dependent interactions determine outcome of competition between two breast cancer cell lines. *Sci Rep* 2021; 11: 1–18.

75. Sgarminato V, Tonda-Turo C, Ciardelli G. Reviewing recently developed technologies to direct cell activity through the control of pore size: From the macro- to the nanoscale. *Journal of Biomedical Materials Research - Part B Applied Biomaterials* 2020; 108: 1176–1185.

76. Downing TL, Soto J, Morez C, et al. Biophysical regulation of epigenetic state and cell reprogramming. *Nat Mater* 2013; 12: 1154–1162.

77. Sung JH, Shuler ML. Microtechnology for mimicking in vivo tissue environment. *Ann Biomed Eng* 2012; 40: 1289–1300.

78. Randriamanantsoa S, Papargyriou A, Maurer HC, et al. Spatiotemporal dynamics of self-organized branching in pancreas-derived organoids. *Nat Commun* 2022; 13: 1–15.

79. Fang Y, Eglen RM. Three-Dimensional Cell Cultures in Drug Discovery and Development. *SLAS Discov* 2017; 22: 456–472.

80. Laschke MW, Menger MD. Life is 3D: Boosting Spheroid Function for Tissue Engineering. *Trends Biotechnol* 2017; 35: 133–144.

81. Van AI, Bulcke D, Bogdanov B, et al. Structural and Rheological Properties of Methacrylamide Modified Gelatin Hydrogels. Epub ahead of print 2000. DOI: 10.1021/bm990017d.

82. Paszke A, Gross S, Massa F, et al. PyTorch: An Imperative Style, High-Performance Deep Learning Library. *Neural Inf Process Syst* 2019; 32.

83. Lee JH, Kim SK, Khawar IA, et al. Microfluidic co-culture of pancreatic tumor spheroids with stellate cells as a novel 3D model for investigation of stroma-mediated cell motility and drug resistance. *J Exp Clin Cancer Res* 2018; 37: 1–12.

84. Jeong SY, Lee JH, Shin Y, et al. Co-culture of tumor spheroids and fibroblasts in a collagen matrix-incorporated microfluidic chip mimics reciprocal activation in solid tumor microenvironment. *PLoS One* 2016; 11: e0159013.

85. Fujiwara M, Kanayama K, Hirokawa YS, et al. ASF-4-1 fibroblast-rich culture increases chemoresistance and mTOR expression of pancreatic cancer BxPC-3 cells at the invasive front in vitro, and promotes tumor growth and invasion in vivo. *Oncol Lett* 2016; 11: 2773.

86. Sgarminato V, Marasso SLL, Cocuzza M, et al. PDAC-on-chip for in vitro modeling of stromal and pancreatic cancer cell crosstalk. *Biomater Sci*. Epub ahead of print 2022. DOI: 10.1039/D2BM00881E.

87. Van Der Weken D, Nachtegael M, Kerre EE. Using similarity measures and homogeneity for the comparison of images. *Image Vis Comput* 2004; 22: 695–702.

88. Preibisch S, Saalfeld S, Tomancak P. Globally optimal stitching of tiled 3D microscopic image acquisitions. *Bioinformatics* 2009; 25: 1463.

89. Abràmoff MD, Magalhães PJ, Ram SJ. Image Processing with ImageJ. *Biophotonics Int* 2004; 11: 36–42.

90. Hunter JD. Matplotlib: A 2D graphics environment. *Comput Sci Eng* 2007; 9: 90–95.

91. Waskom ML. seaborn: statistical data visualization. *J Open Source Softw* 2021; 6: 3021.

92. McKinney W. Data Structures for Statistical Computing in Python. In: *Proceedings of the 9th Python in Science Conference*. SciPy, 2010, pp. 56–61.